The Astrophysical Journal, 999:260 (12pp), 2026 March 10 https://doi.org/10.3847/1538-4357/ae4027
© 2026. The Author(s). Published by the American Astronomical Society.
OPEN ACCESS

The Noneruptive Reconfiguration of a Quiescent Filament After a Nearby Active Region Emergence

James McKevitt[1,2], Louise Harra[3,4], Gherardo Valori[5], Deborah Baker[1], Nils Janitzek[3,4], Stephanie Yardley[1,6,7], Sarah Matthews[1], Hamish A. S. Reid[1], Alexander W. James[1], Muriel Stiefel[4,8], David H. Brooks[1,9], Ryan M. Dewey[10], Jim M. Raines[10], Susan T. Lepri[10], Liang Zhao[10], and Juan Sebastián Castellanos Durán[5]
[1] University College London, Mullard Space Science Laboratory, Holmbury St. Mary, Dorking, Surrey, RH5 6NT, UK; james.mckevitt.21@ucl.ac.uk
[2] University of Vienna, Institute of Astrophysics, Türkenschanzstrasse 17, Vienna A-1180, Austria
[3] Physikalisch-Meteorologisches Observatorium Davos/World Radiation Center, PMOD/WRC, Dorfstrasse 33, Davos Dorf, 7260, GR, Switzerland
[4] D-PHYS, ETH Zürich, Wolfgang-Pauli Strasse 27, Zürich, 8093, ZH, Switzerland
[5] Max-Planck-Institut für Sonnensystemforschung, Justus-vonLiebig-Weg 3, 37077, Göttingen, Germany
[6] Department of Mathematics, Physics and Electrical Engineering, Northumbria University, Ellison Place, Newcastle upon Tyne, NE1 8ST, UK
[7] Donostia International Physics Center (DIPC), Paseo Manuel de Lardizabal 4, 20018, San Sebastián, Spain
[8] University of Applied Sciences and Arts Northwestern Switzerland, Bahnhofstrasse 6, 5210 Windisch, Switzerland
[9] Computational Physics Inc., Springfield, VA 22151, USA
[10] Department of Climate and Space Sciences and Engineering, University of Michigan, 2455 Hayward Street, Ann Arbor, MI 48109-2143, USA
Received 2025 July 3; revised 2026 January 16; accepted 2026 January 31; published 2026 March 9

Abstract

The unpredictability of solar filament eruptions presents major challenges for forecasting space weather, since such eruptions frequently drive coronal mass ejections that impact the heliosphere. While nearby flux emergence is often linked to their destabilization, the specific characteristics of both the emerging flux and the filament that determine whether an eruption occurs remain unclear. We report observations of a quiescent filament that did not erupt following the nearby emergence of active region NOAA 13270 and a subsequent C-class flare in 2023 April. Our analysis combines multiviewpoint extreme ultraviolet (EUV) imaging and X-ray imaging with EUV spectroscopy, radio imaging, and measurements of, and extrapolations from, the photospheric magnetic field. We identify the formation of a coronal null point and fan-spine topology at the interface between the active region and filament which exhibited persistent slow reconnection, indicated by chromospheric brightenings, persistent radio emission, and plasma upflows. Our results indicate that ongoing reconnection and jets can relieve magnetic stress and enable filament stability, even when under strong perturbation. We suggest that the orientation of emerging flux relative to the ambient field is a critical parameter in filament evolution and we provide observational constraints for models of filament stability and eruption.

Unified Astronomy Thesaurus concepts: Solar filaments (1495); Solar magnetic flux emergence (2000); Solar magnetic fields (1503); Solar extreme ultraviolet emission (1493); Solar radio emission (1522); Solar flares (1496)

1. Introduction

Solar filaments, cool and dense structures of plasma in the hotter and more tenuous corona, are a key element of solar activity (J.-C. Vial 1998; S. Parenti 2014). The filament plasma resides within filament channels, structures of highly sheared and/or twisted magnetic fields located above photospheric polarity-inversion lines (S. F. Martin 1998; Y. Wang & K. Muglach 2007). The formation of these filament channels is strongly influenced by magnetic shear at the photospheric level (B. Schmieder et al. 1996). Filaments can become destabilized and erupt, yet they may also withstand considerable photospheric forcing without producing coronal mass ejections (CMEs), making predictions of their eruptive behavior particularly challenging.

Quiescent filaments, typically found far from active regions, are rooted in large-scale, weaker fields associated with decayed active regions (O. Engvold 1998; D. H. Mackay 2015). These filaments experience gradual coronal field stress due to surface shear motions, episodic flux emergence, or flux cancellation, accumulating free magnetic energy that is eventually released either gradually via smaller-scale reconnection events or explosively through large-scale eruptions (S. K. Antiochos et al. 1999). A significant driver of filament activity is the emergence of new magnetic flux associated with active regions.

Observations frequently highlight the crucial role of flux emergence in destabilizing existing coronal structures, including large quiescent filaments and their arcades (e.g., J. Feynman & S. F. Martin 1995). Both statistical analyses and detailed case studies have demonstrated that the formation of a nearby active region often triggers filament eruptions through magnetic interactions between emerging flux and the ambient magnetic environment (e.g., K. S. Balasubramaniam et al. 2011). Magnetic reconnection resulting from these interactions can effectively remove, restructure, or reorient overlying magnetic fields, allowing filament channels to rise and erupt (J. Feynman & S. F. Martin 1995; Y.-M. Wang & N. R. Sheeley 1999; P. F. Chen & K. Shibata 2000).

The emergence of magnetic flux can also drastically alter the coronal magnetic field topology, creating complex magnetic structures such as fan-spine configurations (T. Török et al. 2009; Y. Duan et al. 2024). In their simpler configuration, fan-spine topologies are characterized by a dome-shaped separatrix surface (fan) anchored at the photosphere, with a null point—where the magnetic field strength is

Original content from this work may be used under the terms of the Creative Commons Attribution 4.0 licence. Any further distribution of this work must maintain attribution to the author(s) and the title of the work, journal citation and DOI.

zero—located at the dome apex. Inner and outer spine field lines intersect this null point. The inner spine is typically rooted in a photospheric parasitic polarity, that being flux opposite in sign to its surrounding magnetic environment. Such coronal null points are stable structures which can last for days (M. Luoni et al. 2007) and are preferential sites for reconnection (D. I. Pontin et al. 2011).

Fan-spine reconnection is associated with a variety of solar phenomena, including jets, circular flare ribbons, remote flaring activity, and radio bursts (e.g., S. Masson et al. 2009; H. A. S. Reid et al. 2012; H. Wang & C. Liu 2012; C. Liu et al. 2015; T. Li et al. 2018; Y. Duan et al. 2022, 2024). Observationally, persistent upflows of coronal plasma often mark sites of magnetic reconnection occurring at separatrix footprints and quasi-separatrix layers (QSLs). S. J. Edwards et al. (2016) demonstrated that such upflows frequently coincide spatially with photospheric footprints of null-point separatrices. Complementary work by P. Démoulin et al. (2013) suggests that these upflows arise from a pressure gradient established between reconnecting high-pressure active-region loops and adjacent lower-pressure loops along QSLs. Additional numerical studies indicate similar plasma outflows can be driven simply by active-region expansion (M. J. Murray et al. 2010).

Several mechanisms are proposed for magnetic interactions triggering filament eruptions (see Table 1 of L. M. Green et al. 2018). In the magnetic breakout model, reconnection occurs at a magnetic null point between a sheared filament-channel arcade and adjacent magnetic fields in a multipolar (typically quadrupolar) configuration, removing the overlying, unsheared (strapping) fields and enabling eruption of the core structure (S. K. Antiochos 1998; S. K. Antiochos et al. 1999; C. R. DeVore & S. K. Antiochos 2008; B. J. Lynch et al. 2008). Alternatively, eruption can be triggered by internal tether-cutting reconnection beneath the filament within the sheared core field, which is often facilitated by flux cancellation at the polarity-inversion line (PIL) (R. L. Moore et al. 2001; G. Aulanier et al. 2010; A. C. Sterling et al. 2010). In some cases, suitably oriented magnetic flux emergence near the PIL may promote either internal or external reconnection, injecting axial flux or currents and destabilizing the filament channel (J. Feynman & S. F. Martin 1995; P. F. Chen & K. Shibata 2000; T. Li et al. 2015; S. Dacie et al. 2018; T. Török et al. 2024). Previous studies have found large-scale filament eruptions associated with nearby flux emergence and cancellation but the precise mechanism, whether breakout, internal tether-cutting, or ideal magnetohydrodynamic instability, may vary or act in combination in individual events (G. Aulanier et al. 2010; A. C. Sterling et al. 2010).

Observational studies typically correlate large-scale filament eruptions with nearby flux emergence events, particularly when mutual field orientations favor reconnection (J. Feynman & S. F. Martin 1995; Y.-M. Wang & N. R. Sheeley 1999; T. Török et al. 2024). Nevertheless, several counterexamples highlight that filaments can endure significant magnetic perturbations without erupting (e.g., T. Li et al. 2015; T. Török et al. 2024, and references therein).

Consequently, noneruptive interactions between emerging active regions and quiescent filament channels serve as crucial observational tests for existing eruption models. Understanding why some stressed magnetic configurations remain stable while others lead to eruptions, CMEs, or both requires detailed case studies connecting photospheric magnetic evolution, coronal magnetic field topology, and observational signatures of magnetic reconnection.

In this study, we examine one such noneruptive example between 1 and 7 April 2023, whereby a bipolar active region (NOAA 13270) emerged adjacent to a pre-existing filament channel, creating a null point and associated separatrix dome between the newly formed and surrounding ambient fields. We investigate the corresponding signatures of reconnection, including persistent plasma upflows, electron beam indicators, and notable filament reconfiguration. We also analyze the largest flare from this active region—a C-class flare on April 6—which is not associated with the eruption of the filament.

This paper is structured as follows. In Section 2, we present an overview of the observations and instruments we use in this study. In Section 3, we show in detail the emergence of the active region nearby the filament and the resulting activity and magnetic topology. In Section 4, we discuss the changes in magnetic topology during the interaction and explore the reasons the filament was not destabilized. In Section 5, we present our conclusions.

2. Overview of Observations

We used ground-based, Earth-orbiting, and Sun-orbiting instruments in our study. These are summarized in Table 1 and detailed in this section.

2.1. Extreme Ultraviolet Imaging: Coronal Structure and Evolution

We used multiwavelength extreme ultraviolet (EUV) imaging to track the temporal evolution of coronal structures and identify signatures of magnetic reconnection. The Atmospheric Imaging Assembly onboard the Solar Dynamics Observatory (SDO/AIA; J. R. Lemen et al. 2012; W. D. Pesnell et al. 2012) provided continuous full-disk observations from Earth's perspective for the duration of our study. SDO/AIA's multiple temperature channels enabled us to distinguish between cool filament material (304 Å; $\log T \sim 4.7$), coronal loops at various temperatures (171 Å; $\log T \sim 5.8$, 193 Å; $\log T \sim 6.2$ and 7.3), and hot flare plasma (94 Å; $\log T \sim 6.8$).

Complementary EUV imaging from the Extreme Ultraviolet Full-Sun Imager onboard Solar Orbiter (SO/EUI-FSI; D. Müller et al. 2020; P. Rochus et al. 2020) provided a second viewpoint up to 42° ahead of Earth relative to the Sun's rotation (shown in Figure 1). This enabled us to resolve foreshortening effects that affected Earth-based observations later in the study, particularly for determining the spatial relationship between the active region and filament structures. We used the 174 and 304 Å channels, which observe mostly ∼1 MK coronal plasma and ∼0.1 MK chromospheric and transition region plasma, respectively (e.g., Y. Chen et al. 2021; L. A. Hayes et al. 2024).

2.2. Extreme Ultraviolet Spectroscopy: Plasma Flows

To identify and quantify plasma flows indicative of magnetic reconnection, we analyzed spectroscopic observations from the EUV Imaging Spectrometer on Hinode (Hinode/EIS; J. L. Culhane et al. 2007; T. Kosugi et al. 2007). We focused primarily on the strong Fe XII 195.119 Å (∼1.6 MK) coronal emission line, which provides reliable Doppler measurements in typical active region plasma. We

Table 1
Summary of Instruments Used in This Study

Instrument	Platform	Location/Orbit	Function	Observable
Ground-based				
Radioheliograph	Nançay Radio Obs.	Earth	Radio imaging	Particle acceleration
Earth-orbiting				
AIA	SDO	Geosynchronous	EUV imaging	Atmospheric structure and evolution
HMI	SDO	Geosynchronous	Magnetograms	Photospheric magnetic field
XRS	GOES-16	Geostationary	X-ray flux	Flare timing
EIS	Hinode	Sun-synchronous	EUV spectroscopy	Coronal plasma flows
XRT	Hinode	Sun-synchronous	Soft X-ray imaging	High energy release
Sun-orbiting				
EUI-FSI	Solar Orbiter	$\leqslant 42^\circ$ ahead of Earth	EUV imaging	Atmospheric structure and activity
STIX	Solar Orbiter	$\leqslant 42^\circ$ ahead of Earth	Hard X-ray imaging	High energy release

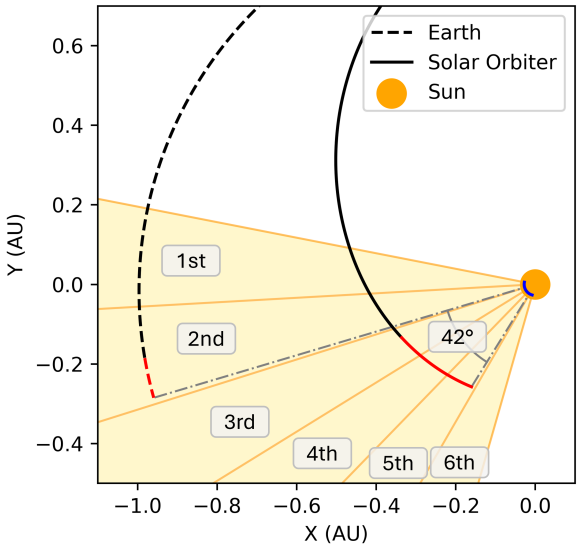

Figure 1. The positions of SO and Earth, viewed from above the ecliptic plane. Their locations for the period from 00:00 UT on 2023 April 1 to 00:00 UT on April 7 are highlighted in red. The active region's path on the solar surface between these times is shown in blue, and a yellow line projects radially from the center of the active region for the dates of the study.

also analyzed observations at higher temperatures using the Fe XVI 262.984 Å emission line (∼2.5 MK).

We derived line-of-sight Doppler velocities by fitting Gaussian profiles to the emission lines using the `MPFIT` algorithm (C. B. Markwardt 2009) implemented in the EIS Python Analysis Code (EISPAC; M. J. Weberg et al. 2023). The Doppler velocity v was calculated from the fitted line centroid λ, rest wavelength λ_0, and speed of light c using $v = c\frac{\lambda - \lambda_0}{\lambda_0}$.

2.3. Photospheric Magnetograms: Magnetic Field Observations and Extrapolations

We tracked the emergence and evolution of photospheric magnetic flux using magnetograms from the Helioseismic and Magnetic Imager on SDO (SDO/HMI; J. T. Hoeksema et al. 2014). Where vector magnetic field data were used, these were disambiguated using the minimum energy method (T. R. Metcalf 1994; T. R. Metcalf et al. 2006) for active region fields and the radial acute method for quiet Sun regions.

To understand the three-dimensional coronal magnetic topology and identify sites of potential reconnection, we performed nonlinear force-free field (NLFFF) extrapolations using the photospheric vector magnetograms. Details of our vector potential-based NLFFF method are provided in the Appendix. We identified QSLs—volumetric structures where magnetic connectivity changes rapidly—by calculating squashing factor Q-maps from our extrapolated fields using the `QSL Squasher` implementation (S. Tassev & A. Savcheva 2017). High Q values indicated strong field line divergence characteristic of separatrix surfaces and potential reconnection sites.

2.4. Radio Imaging: Particle Acceleration

To identify sites of persistent particle acceleration associated with magnetic reconnection, we analyzed radio imaging from the Nançay Radioheliograph (NRH; A. Kerdraon & J.-M. Delouis 1997). The NRH's interferometric observations at frequencies between 150 and 445 MHz enabled us to track type I noise storms, which indicate quasi-continuous electron acceleration in the low corona (K. Kai et al. 1985).

2.5. X-Ray Imaging: High Energy Release

We used multiviewpoint complementary X-ray observations to pinpoint the location of hot plasma generated by the C3.9-class flare on April 6. The Spectrometer Telescope for Imaging X-rays onboard SO (SO/STIX; S. Krucker et al. 2020) provided hard X-ray imaging (4–150 keV) sensitive to hot flare plasma ($\gtrsim$10 MK). We reconstructed the flare morphology using SO/STIX forward-fitting routines (A. Volpara et al. 2022).

Soft X-ray observations from the X-Ray Telescope on Hinode (Hinode/XRT; L. Golub et al. 2007) using the Be-med filter provided complementary imaging of thermal emission from ∼10 MK flare loops. The combination of SO/STIX and Hinode/XRT observations, obtained from different viewing angles, enabled us to identify the three-dimensional location of the flaring arcade relative to the filament.

2.6. X-Ray Flux: Flare Timing and Classification

Flare timing was determined using X-ray flux measurements from the X-ray Sensor (XRS) on the GOES-16 spacecraft (T. N. Woods et al. 2024), which provided the standard GOES classification and temporal profile of the event.

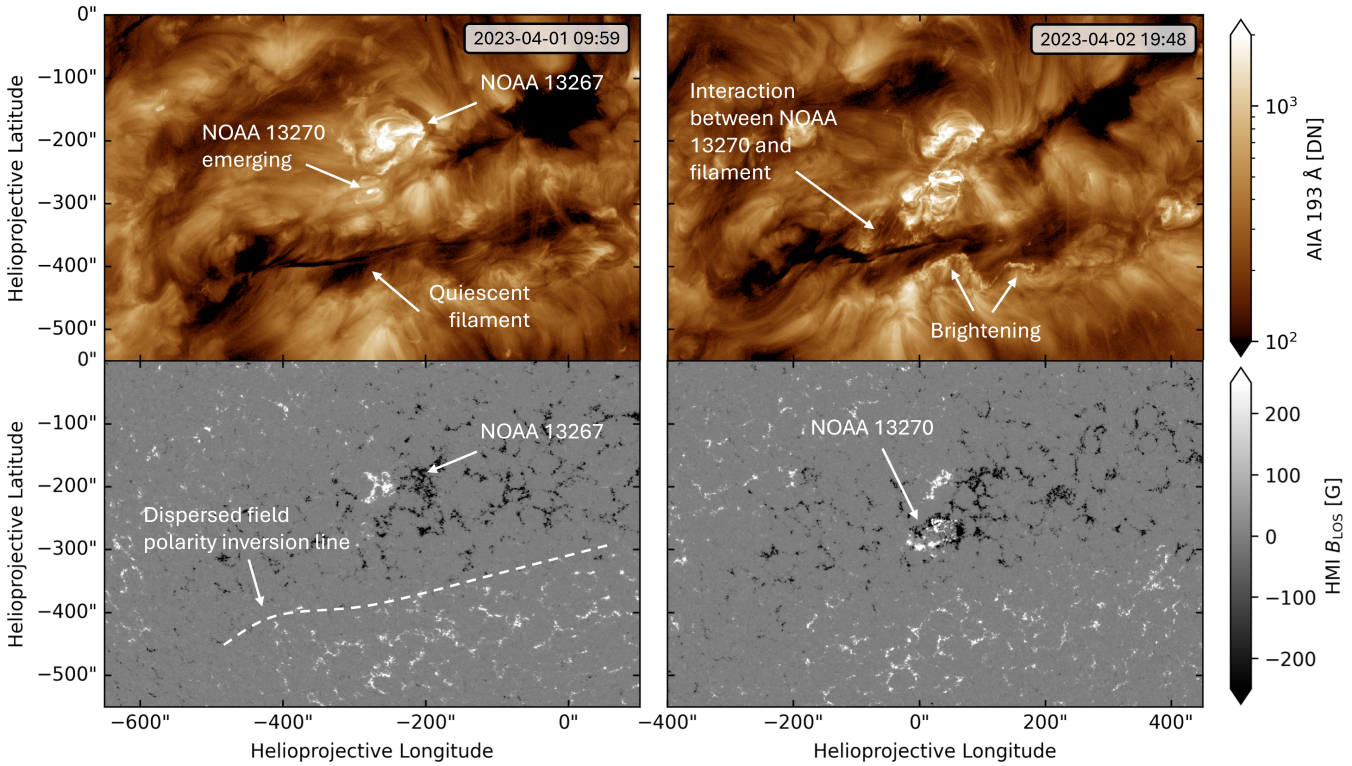

Figure 2. Observations of the emergence of NOAA 13270 on April 1(left) and the subsequent remote brightenings on April 2(right). Coronal plasma as seen by SDO/AIA in the 193 Å channel is shown in the top row, and the line-of-sight photospheric magnetic field measured by SDO/HMI is shown in the bottom row.

3. Results

3.1. April 1 and 2: Emergence

On 2023 April 1, a large quiescent filament extended around 500″ from just south of disk center to the east, as seen from Earth. The filament channel was formed by a large dispersed positive polarity to the south and a large dispersed negative polarity to the north. Active region NOAA 13267 was on the northern edge of that negative polarity.

At approximately 10:00 UT on April 1, small-scale EUV activity associated with the emergence of new active region NOAA 13270 was detected. We show this with observations of the coronal plasma in the left panel of Figure 2. The emergence of NOAA 13270 did not appear to immediately coincide with any notable changes to the surrounding corona, and continued at this low level for approximately 1 day.

Significant magnetic flux emergence forming NOAA 13270 then began at around 10:00 UT on April 2 and continued for many days. This was not initially accompanied by any noticeable brightening anywhere other than the core of the new active region. By approximately 20:00 UT, continued emergence of photospheric magnetic flux had caused the active region to expand. At the same time, remote brightenings south of the filament were observed. We show these brightenings in the coronal plasma in the right panel of Figure 2. These brightenings persisted for many days and traced a line mostly parallel with the filament channel on the south side, consistent with the footpoint location of retaining (strapping) unsheared arcades which typically accompany filament channel structures.

At this time, the different active region polarities had not yet formed distinct bipoles at the photosphere (see the bottom right panel of Figure 2). Combined with still being small, this led to the photospheric field generating a complex and low-lying coronal magnetic field topology which dominated the immediately surrounding coronal magnetic field but did not appear to be extensive enough to exert an influence on the surrounding field containing the filament channel.

3.2. April 3, 4, and 5: Entanglement

3.2.1. EUV Imaging

As the active region emergence continued, a partial circular ribbon formed in the chromosphere to the east of NOAA 13270. We show this at 00:00 UT on April 3 in the left panel of Figure 3. The emerging active region is bipolar, where the negative polarity is leading to the west and the positive polarity is trailing to the east. Since the active region emerged into a large area of dispersed negative magnetic flux, its eastern trailing positive polarity is, therefore, parasitic in nature.

The circular chromospheric ribbon to the east of the new active region is consistent with the formation of a null point and separatrix dome above the trailing positive polarity, since it is connected to the surrounding negative magnetic flux. Slow steady reconnection at the null point would provide energy to the plasma which would be seen in the ribbon (S. Masson et al. 2009). As the positive polarity grew with the emergence of more positive photospheric magnetic flux, the boundary of the circular ribbon also grew. This is consistent with the growth of a seperatrix dome encompassing more balancing negative ambient magnetic field.

The middle panel of Figure 3 shows a strong filament activation taking place shortly after the appearance of the

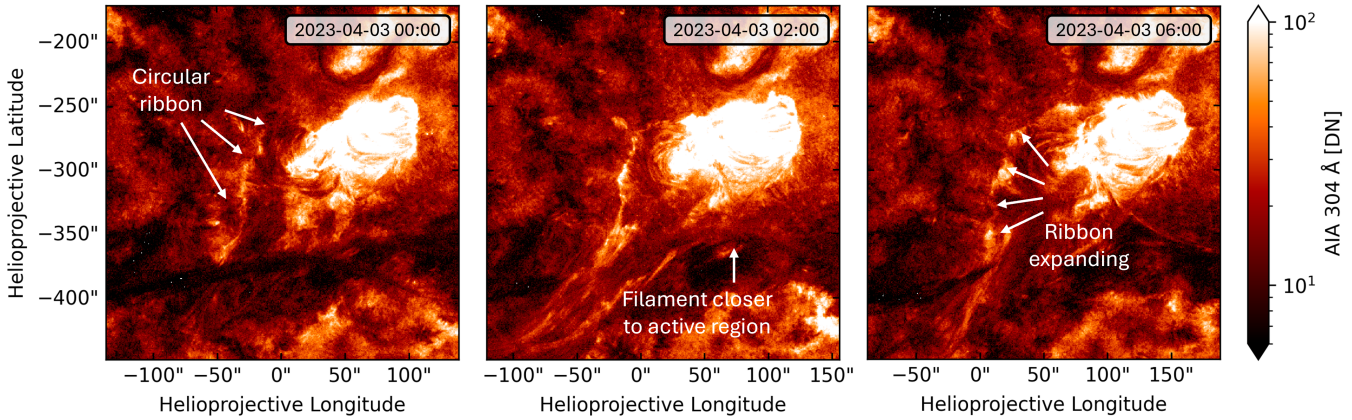

Figure 3. Observations of the expanding circular ribbon around the east side of NOAA 13270 and the movement of the filament material on April 3 as seen in the SDO/AIA 304 Å channel. This figure is available as an animation. The animation runs from 2023 May 3 00:00:17 to the same day at 05:59:53. The real-time duration of the animation is 40 s.

circular ribbon. The filament activation proceeded down the eastern side of the filament originating in the active region. At the same time, dark, cooler filament material is seen displaced closer to the active region. This change of the filament position is not accompanied by any flare or sign of strong reconnection. However, it appears from these observations that active region plasma enters the filament channel at this point of interaction.

Following this, flux emergence continued and the circular ribbon expanded further. At the same time, the filament was disrupted and a complete entanglement of the active region and the filament began. We show this in the right panel of Figure 3. This is consistent with a separatrix fan boundary expanding, meeting, and then interacting with the filament channel. At this time, the active region does not cause disruption of the surrounding field sufficient to eject or cancel the filament channel. However, the filament channel does appear to be displaced northward toward the active region.

3.2.2. NLFFF Extrapolations

We perform an NLFFF extrapolation on April 3 to analyze the coronal magnetic topology more closely at this particularly critical point in time. Our extrapolation can be seen in Figure 4. Our modeling shows a magnetic fan structure (yellow) around the positive polarity of NOAA 13270 corresponding with the radius traced by the circular ribbons seen in Figure 3. Additionally, the twisted filament channel field lines (blue) also appear to trace a radius around this emerged positive polarity for some distance and toward the active region PIL, before returning to the field's primary PIL. The retaining (strapping) high-altitude arcades (green) appear to have separated around the separatrix boundary and the lower-level arcades (red) show shear to match the curvature of the filament channel.

Continuing with the analysis of the observations, several hours after this reconfiguration we see remote brightening east of the active region and continued filament activation as active region plasma enters and propagates eastward along the filament channel. In order to investigate possible topological consequences of this process, we performed an NLFFF extrapolation of the region at this time on April 4 and found that the null point was now magnetically connected to the filament channel. We show our extrapolation in Figure 5. Additionally, the high-altitude filament-retaining (strapping) field (green) continues to be separated above the null fan boundary to the north of the active region, and the lower-level retaining (strapping) field (orange), connected to the photosphere at the south, appears connected to the null point and to the north of the active region.

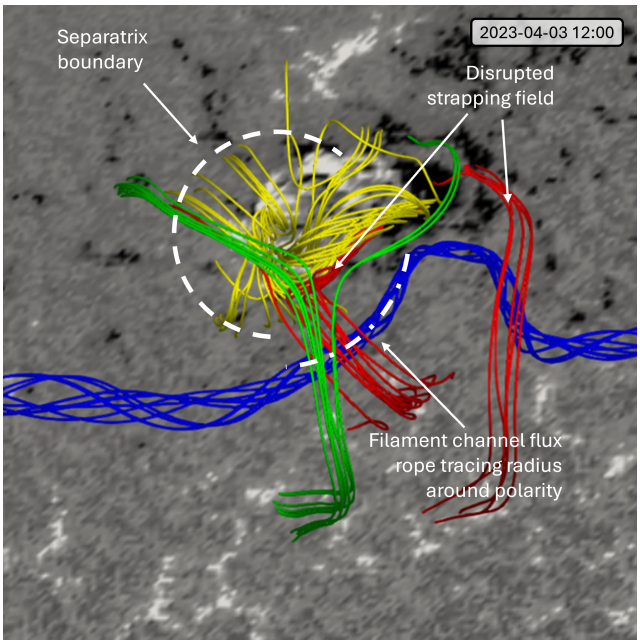

Figure 4. NLFFF extrapolation of the photospheric vector magnetic field measured by SDO/HMI on April 3. The flux rope at the core of the filament channel is shown in blue, the overlying field in red, the null fan in yellow and the higher strapping field in green. The viewpoint is oriented to match that of Earth.

3.2.3. Spectroscopic and Radio Data

On April 4 the cool plasma of the filament channel became difficult to trace at the active region location in EUV imaging, and the path of the filament past the active region became unclear. The left panel of Figure 6 shows that a strong source of 432 MHz radio emission on April 4, the strongest on the whole disk at that time, is concentrated at the same location where the coronal null point was present in our NLFFF extrapolations, above the positive polarity of the active region.

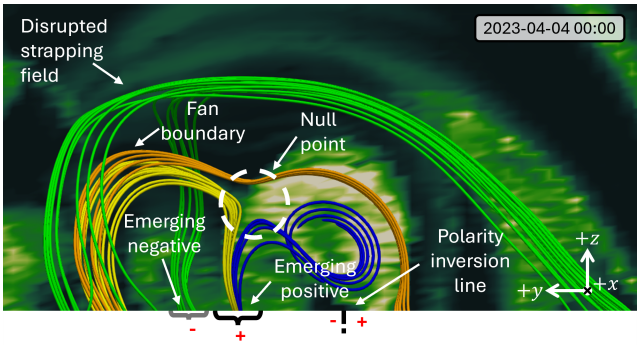

Figure 5. NLFFF extrapolation of the photospheric vector magnetic field measured by SDO/HMI on April 4. The high-altitude strapping field is shown in green, lower-level overlying field in orange, field originating at the new positive polarity and, via a null point forming part of a fan topology in yellow, and field originating in the new positive polarity connected via the null point to the filament channel in blue. A Qmap showing $\log Q$ in the y–z plane at the null point is shown, with the colors placed behind the field lines for visibility, and where brighter regions are those of high Q values.

The radio signal is indicative of a type I noise storm that is driven by energetic electrons being quasi-continuously accelerated in the low corona, in areas of plasma density around $10^{9.5}\,\mathrm{cm}^{-3}$ assuming fundamental emission, where the observed radio frequency corresponds to the local plasma frequency (e.g., G. A. Dulk 1985). We do not observe the radio type I emission at the lower frequencies around 150 MHz, indicating that the accelerated particles do not have access to larger magnetic loops than around 0.4 solar radii in altitude, based on the plasma density scale height in the corona (e.g., G. Mann et al. 1999). The radio emission began on April 3 but became consistently strong on April 4. Some low-lying bright loops also appear to connect south from the active region as it further expands. It is at that time that NOAA 13270 had grown to additionally become entangled with NOAA 13267.

Late on April 5, Hinode/EIS observed persistent plasma upflows of 10–35 $\mathrm{km\,s}^{-1}$ in the plasma at the coronal Fe XII 195.119 Å ($\log T_{\max} = 6.2$) and hot Fe XVI 262.984 Å ($\log T_{\max} = 6.4$) emission lines. The location of the upflowing plasma was identical in both cases, and is shown for Fe XII 195.119 Å in the right panel of Figure 6 on April 5. While slightly affected by the Hinode/EIS field of view, these measurements were sufficient to determine that the upflowing plasma coincided with the strong continuous 432 MHz radio emission and the location of the extrapolated null point. Hinode/EIS continued to observe upflowing plasma of similar velocity from this same location until April 7, when the active region was too close to the limb to be followed further.

April 5 was the start of a more severe displacement of the eastern side filament away from its original location, seen in the right panel of Figure 6. It is unclear from observations at this point in time, given the brightness of the active region plasma, whether the filament channel maintains an uninterrupted coherent structure with a single axis past or through the active region core, or whether there is some disconnection between the east and west sides of the filament, with the west side remaining more undisturbed than the east. We speculate further over such possibilities in Section 4.

3.3. April 6 and 7: Jets and Flare

Early on April 6, the relative position of the filament material to the east and west of the active region was largely unchanged. Using EUV imaging, it remains indiscernible whether a continual filament channel passes through or past the active region, or whether what we see is simply the two ends of new, separate filament channels. The filament material on the eastern side of the active region remained elevated and more northern, while the west filament material remained radially above the ambient field's PIL. Around this time, numerous jets are seen on the eastern side of the active region, an example of which we show at 02:30 UT on April 6 in the bottom panel of Figure 7. The jet appears to originate slightly south of the filament material to the east of the active region.

At approximately 14:00 UT on April 6, a GOES C3.9-class flare occurred. It lasted until 14:29 UT and caused associated EUV brightenings in the surrounding plasma that persisted for several hours. To determine the three-dimensional location of the energy release relative to the filament, we combined EUV imaging with X-ray observations from two viewpoints at Earth and from SO further around the Sun (see Figure 1).

We show the flare topology in Figure 8 by overlaying the location of the hot X-ray emitting plasma onto images of EUV emission. The left and right panels show the view from Earth. Here, the soft X-ray emission observed by Hinode/XRT (green contours) identifies the hot thermal plasma. This emission is cospatial with hot loop structures seen in the SDO/AIA 94 Å channel ($\log T \sim 6.8$), and so we annotate all the panels of this figure with this AIA 94 Å/XRT loop in red. The central panel shows the view from SO using SO/EUI-FSI 174 Å. The blue contours in this panel represent the location of the peak X-ray intensity reconstructed from SO/STIX data. We plot the three-dimensional loop geometry derived from the SO/STIX forward-fitting analysis on all panels with a blue line, which aligns well with the AIA 94Å/XRT loop.

The combined viewing angles strongly suggest that the flaring structure is an arcade overlying the filament channel, rooted in the dispersed positive field south of the filament and in negative polarity of the active region to the north. This is consistent with energy deposition at the arcade footpoints seen in the brightening EUV ribbons parallel to, and south of, the filament which appeared at the same time as the flare, shown in the center and right panels.

The filament remained stable in position despite the flare.

4. Discussion

4.1. Topology of the Emerging Active Region

The interaction between the emerging bipolar active region NOAA 13270 and the pre-existing quiescent filament channel shows a complex evolution of topology. Our observations and extrapolations consistently show that a fan-spine separatrix layer formed around the positive polarity of NOAA 13270, which acted as a parasitic polarity embedded in the surrounding ambient negative field. In the extrapolation, the fan separatrix also appeared to exhibit an asymmetry in the density of its magnetic footpoints at the photosphere, which can be expected to yield a correspondent asymmetry in the energy density deposition from the reconnection outflows along the fan. This is consistent with the observed appearance of partial circular ribbons in the chromosphere.

As magnetic flux continued to emerge, we observed signatures of the expansion of the separatrix fan, causing a

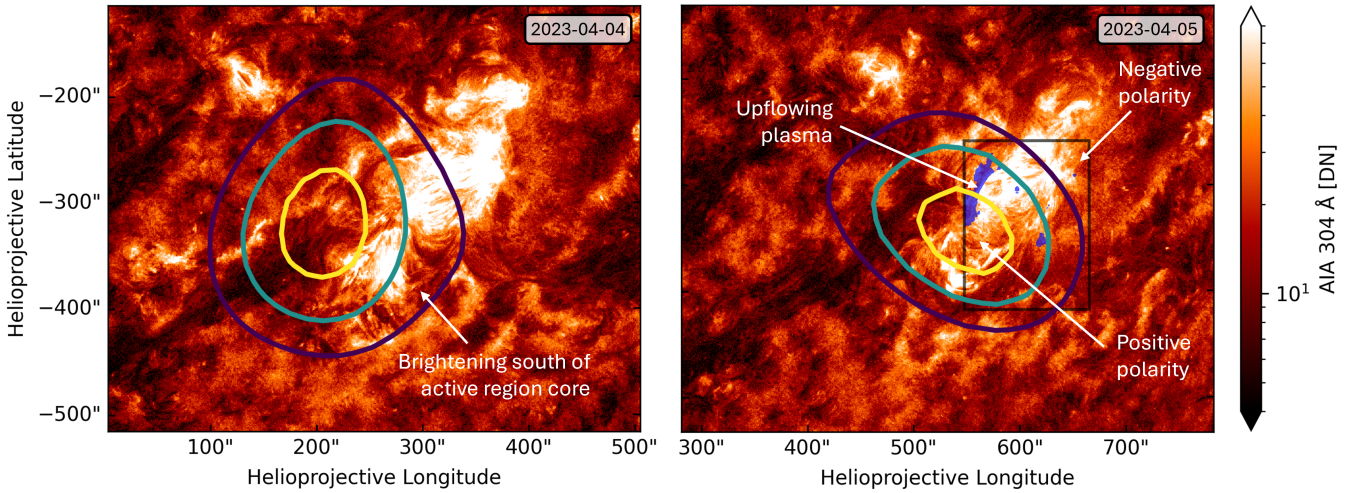

Figure 6. EUV imaging observations of NOAA 13270 using the SDO/AIA 304 Å channel, taken at 07:30 UT on April 4 (left) and 22:05 UT on April 5 (right). Upflowing plasma between 10 and 35 km s^{-1} observed by Hinode/EIS in Fe XII 195.119 Å is also overlaid in blue (right) at the time of the AIA observation, where the field of view of Hinode/EIS is outlined with a translucent black box. Contours showing 432 MHz radio emission between 75% and 95% of the peak strength are overlaid. These were taken on 10:01 UT on April 4 (left) and 15:07 UT on April 5 (right), the closest available steady radio data, and corrected for solar rotation.

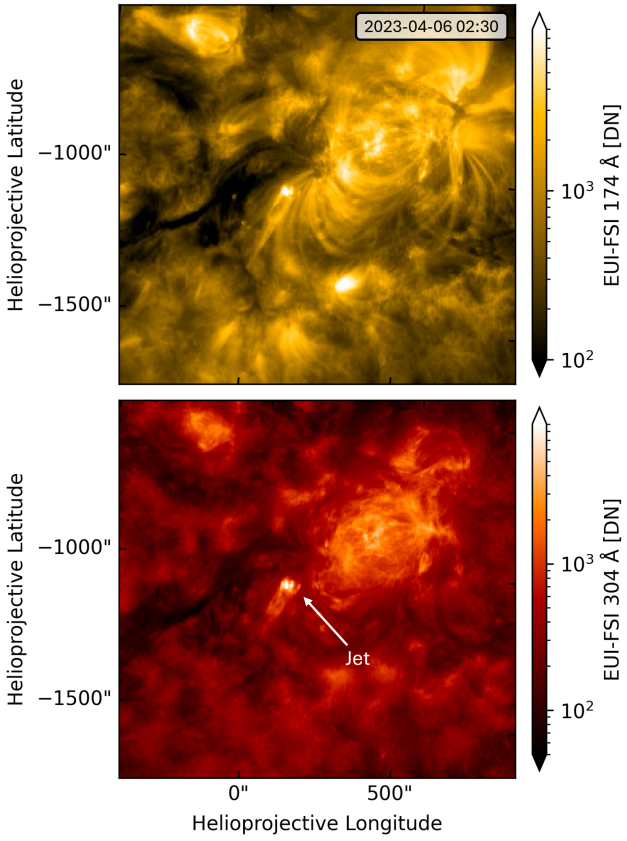

Figure 7. Observations of a jet on the east side of NOAA 13270 as seen by SO/EUI-FSI.

lateral expansion of the partial circular ribbons to progressively encompass more of the surrounding dispersed negative magnetic flux.

Reconnection at the null point, as described by D. I. Pontin et al. (2011), likely provided a source of persistent energy release into the coronal plasma throughout the period studied here, which we observed as chromospheric brightening at the fan's footprint and, once connected to the filament channel, as a continual source of filament activation. Importantly, the null point did not collapse into a current sheet according to our NLFFF extrapolations, as has been seen in the past (D. Pontin 2011).

4.2. Filament Activation and Magnetic Reconfiguration

The growing of the separatrix fan then likely directly interacted with the adjacent filament channel once expanded sufficiently, inducing the significant filament activation seen by hot plasma propagating through the filament from the active region. This represented the first of several perturbations caused by the emerging active region without causing the filament eruption or complete reconfiguration.

Our coronal field extrapolations found the filament's magnetic axis curved around the active region's positive polarity, deviating from its initial alignment along the ambient field's PIL. As we discuss in more detail in Section 4.8, this bending may have arisen because the parasitic polarity displaced the strapping field's anchoring region on one side of the filament channel, forcing reconfiguration and reducing magnetic pressure on the northern side of the filament. This reduction was balanced by the separatrix layer's magnetic pressure at the positive polarity, while the strapping field became sheared at the negative polarity, drawing the filament closer to the active region. The accompanying remote brightenings, south of the active region, then occurred in the same polarity as that of the parasitic polarity, as in the case seen by H. Wang & C. Liu (2012). This partial tracing of a radius around the positive parasitic polarity is similar to the circular filament observed by S. Dacie et al. (2018), in that twisted filament channel field lines can curve along their axial direction around a parasitic polarity.

The same magnetic field extrapolation found the overlying strapping field separated on the northern side of the filament—likely a result of the southern-rooted field losing its northern counterpart due to the emerged negative polarity. Such an opening of magnetic flux can facilitate filament eruption (e.g.,

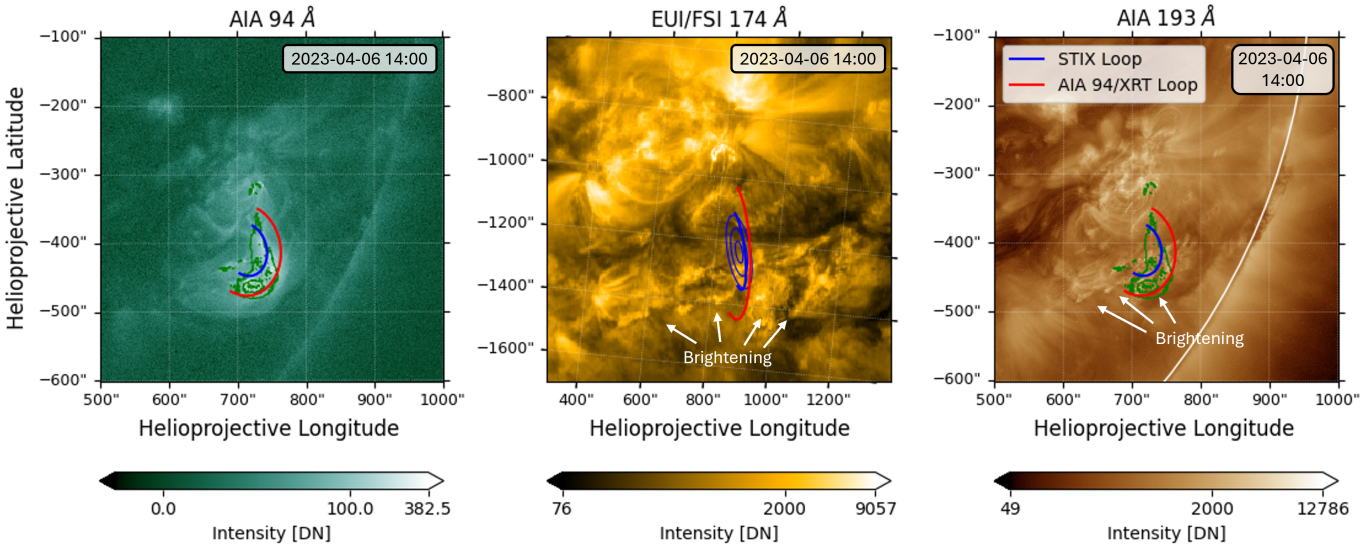

Figure 8. EUV imaging observations of the C3.9 flare on April 6 seen by the SDO/AIA 94 Å (left) and 193 Å (right) channels, and around the Sun from Earth by SO/EUI-FSI 174 Å (center). We overlay intensity contours at 30%, 60%, and 90% of the peak value from Hinode/XRT in green, and those same contours for SO/STIX in blue. We overlay the flaring loop identified by SDO/AIA 94 Å and Hinode/XRT in red, and the flaring loop identified by SO/STIX in blue.

Y.-M. Wang & N. R. Sheeley 1999). However, the filament did not erupt, meaning that no large-scale eruptive mechanism, such as breakout (S. K. Antiochos 1998) or tether-cutting (R. L. Moore & G. Roumeliotis 1992), was successfully triggered.

4.3. Radio Emission and Persistent Plasma Upflows

Following entanglement with the filament channel, the active region null point appeared to persist, coinciding with strong and persistent radio emission at 432 MHz. Similar radio signatures observed at null points by Y. Duan et al. (2022) were attributed, as here, to slow, steady reconnection at such sites. This reconnection would provide continual particle acceleration that drives radio emission such as we see here, along with heating that would drive ongoing filament activation and chromospheric brightening at the separatrix fan's footprint, which we observed.

Persistent plasma upflows (10–35 km s^{-1}) were observed in coronal (Fe XII) and hotter (Fe XVI) emission lines at the location of the radio emission and near the likely null point. While such upflows are routinely associated with active regions (e.g., D. H. Brooks et al. 2021; H. Tian et al. 2021), in this case it is noteworthy that strong upflows persist despite significant interaction with a large-scale filament channel, which could reasonably be expected to influence or disrupt typical active-region dynamics. The persistence of these strong upflows indicates that active regions inherently produce such flows even when embedded within complex, larger-scale coronal topologies.

While the plasma upflows showed structure broadly cospatial with the separatrix layer we suggest is present, Hinode/EIS's limited spatial resolution makes it challenging to pinpoint the precise mechanism driving them conclusively. Future plasma spectrometers such as SOLAR-C/EUVST will enable observations of such dynamics at unprecedented spatial resolution, significantly improving our understanding of these dynamics (T. Shimizu et al. 2019; J. McKevitt et al. 2025).

4.4. Jets as Minifilament Eruptions

We observed numerous jets adjacent to the filament–active region complex following their interaction. A. C. Sterling et al. (2015), supported by P. F. Wyper et al. (2017), proposed that such jets represent small-scale eruptions of sheared magnetic fields ("minifilaments") meaning that in our case such sheared field is continually ejected from the region. These frequent, small eruptions may effectively relieve the accumulated magnetic shear and currents from the coronal field, which would contribute to the stability of the larger filament structure which we see here.

4.5. Flare Dynamics and Filament Stability

A C-class flare on April 6 represented the peak energy release during our observations but notably was not associated with filament eruption. X-ray and EUV imaging (SDO/AIA, SO/STIX, Hinode/XRT) localized the flare within the strapping field overlying the filament rather than within highly sheared fields beneath it, as would be the case for an eruption (R. L. Moore & G. Roumeliotis 1992; S. K. Antiochos 1998).

4.6. Filament Integrity and Potential Fragmentation

As the region moved to the edge of the limb beyond April 6, despite prolonged magnetic perturbations, it remains unclear whether the filament maintained continuity across the active region or fragmented into two intermediate filaments anchored near the active region. EUV observations indicated elevation and northward displacement of the eastern filament segment, suggesting possible partial disconnection or weakening of filament integrity. Such fragmentation reflects nuanced filament responses to strong but localized perturbations, complicating eruption predictions.

The question of filament continuity remains open due to the limitations of magnetic field extrapolation methods at significant distances from the disk center. This highlights the need for high-resolution, multiviewpoint magnetic observations (e.g., via SO/PHI-FDT; G. Valori et al. 2023) to resolve

the detailed quiet Sun photospheric magnetic field underpinning such scenarios.

4.7. Comparison to Previous Studies and Theoretical Implications

J. Feynman & S. F. Martin (1995) described emergences into dispersed single-polarity regions, such as we consider here, as neither favorable nor unfavorable for reconnection, events equally likely to erupt or remain stable and relatively rare observationally.

The interaction studied here aligns partially with previous flux emergence reports (e.g., Y.-M. Wang & N. R. Sheeley 1999; S. Dacie et al. 2018; T. Török et al. 2024) but notably diverges by not producing a large-scale eruption. The work by S. Dacie et al. (2018) on an eruptive case considers emerging elongated bipoles with a PIL parallel to that of the ambient field. This contrasts with our noneruptive case in which the active region PIL is perpendicular to that of the ambient field.

It would be interesting to see if any correlation is present in a statistical study of those emergences into the dispersed single-polarity regions referred to by J. Feynman & S. F. Martin (1995), considered alongside the orientation of the PIL of the emerging field with respect to that of the ambient field.

Our observations provide an interesting perspective on the two-step reconnection scenario proposed by J. Wang & Z. Shi (1993), wherein continuous, relatively slow reconnection, observed as flux cancellation at the photosphere, builds magnetic complexity into large magnetic structures in the corona before energy release takes place in the corona. In our case, continuous reconnection at the null point releases energy from the magnetic field without triggering an eruption and jets potentially release shear from the field without an eruption of the large-scale filament.

4.8. Cartoon Model

To illustrate our interpretation of the observed interactions, we present a cartoon model (Figure 9) corresponding to the observed coronal plasma and the magnetic topologies we model in Figures 4 and 5.

In panel (a), we show the initial magnetic configuration prior to significant interaction. A flux rope associated with the filament channel lies along a dispersed field PIL, stabilized by strapping fields from the surrounding ambient field. The emergence of new magnetic flux from NOAA 13270 introduces a quasi-parasitic polarity, forming a fan-spine topology characterized by a dome-shaped separatrix surface (the fan) and an associated coronal null point. This newly emerged configuration, embedded within the existing dispersed negative polarity region, creates a coronal null point offering a favorable site for reconnection.

Panel (b) illustrates the expansion of the null fan as continued flux emergence injects positive polarity flux into the corona. This rapid expansion disrupts and separates portions of the strapping field originally stabilizing the filament channel. Importantly, the remaining connected strapping field lines still anchor into the dispersed negative field region, thus drawing the filament channel field lines beneath the expanding null fan surface toward the region of lower magnetic pressure generated by the emergence.

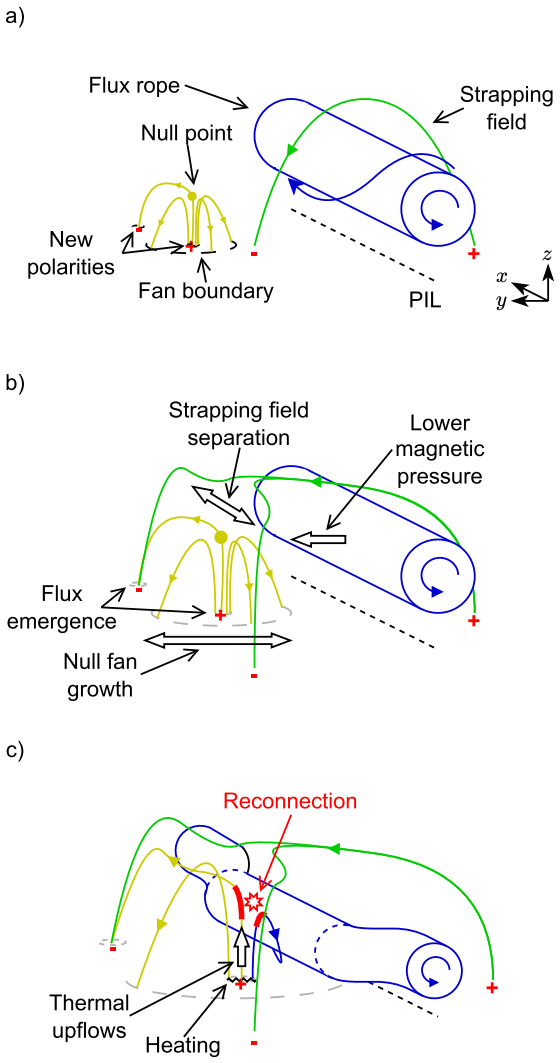

Figure 9. A proposed cartoon model for the interaction between the active region and filament channel. The filament channel (flux rope; blue) initially resides above the ambient field's PIL next to a null fan (yellow) in (a), the strapping field (green) is separated (b), and the channel is then seen connected to the null point reconnection site (c). The colors correspond to those used in Figures 4 and 5.

Finally, in panel (c), we illustrate the resulting persistent magnetic reconnection occurring near the null point, causing upflowing plasma and continuous particle acceleration. The connection between this reconnection site and the filament channel is responsible for the continual activation of the filament.

5. Conclusions

In this work, we analyze why a quiescent filament remained stable despite major magnetic disturbances from the emergence of NOAA 13270.

The first signatures of the emergence of active region NOAA 13270 on 2023 April 1 produced localized EUV activity and no disturbance to the large nearby quiescent filament. By April 2 following the emergence of more photospheric magnetic flux, we observed remote EUV brightenings on the opposite side of the filament, indicating that the emerging flux had begun interacting with the unsheared arcades retaining the filament. As the emergence continued, we

identified the appearance and expansion of a partial circular ribbon near NOAA 13270. We find its behavior is consistent with the formation of a separatrix structure around the emerging positive polarity, which acted as a parasitic polarity within the surrounding negative magnetic flux.

By April 3–4, the filament and emerging flux became fully entangled. We performed NLFFF magnetic field extrapolations and found a seperatrix surface and associated null point above the emerging positive polarity, consistent with the observed circular ribbon. Our extrapolations also found magnetic connectivity between this inferred null point and the filament channel itself, consistent with the signatures we observed of the apparent injection of hotter plasma into the filament channel from the active region. We also detected a strong, spatially stable 432 MHz radio source above the emerging positive polarity, indicative of particle acceleration caused by ongoing magnetic reconnection at a null point.

Later, on April 5, Hinode/EIS measurements of bulk plasma motion found coronal and hot-plasma upflows of 10–35 km s^{-1} cospatial with the radio source and the extrapolated null point location. These upflows are consistent with long-duration, gradual energy release. At this time, the filament was still in place and largely stable with the active region embedded in it despite the emergence of flux at the photosphere and growth of NOAA 13270, ongoing reconnection at the null, and coronal activity. On 6 April, a sequence of jets occurred near the filament–active region interface. Current literature suggests such jets are the ejection of "minifilaments." This would help explain the noneruption of our filament in this case, in that the jets may have contributed to relieving magnetic stress from the system.

Our multiviewpoint analysis of a confined C3.9 flare on April 6 finds it to be located in the overlying strapping loops and not beneath the filament, likely contributing to the stability of the filament during the event.

At every stage, the system appears to have evolved through slow reconnection, topological adjustment, and shear-relieving small-scale ejection, rather than the explosive mechanisms required to destabilize and erupt the filament. In comparison with previous eruptive studies, the emerging flux here was perpendicularly oriented relative to the filament channel, something we suggest is an important parameter in determining the stability of the filament.

Acknowledgments

We are thankful to the referee for the comments and suggestions that helped to improve the manuscript. J.M. was supported by STFC PhD Studentship number ST/X508858/1. S.L.Y. is grateful to the Science Technology and Facilities Council for the award of an Ernest Rutherford Fellowship (ST/X003787/1). H.A.S.R. was supported by UKSA grant ST/X002012/1, and H.A.S.R. and A.W.J. by STFC grant ST/W001004/1. S.M. and D.B. acknowledge support from UKSA grant No. UKRI920. H.A.S.R. and D.B. were supported by UKSA grant No. UKRI980. S.M. was also supported by ESA Contract No. 4000141160/23/NL/IB. R.M.D. was supported by NASA contract NNG10EK25C. L.Z. acknowledges support from NASA grant 80NSSC22K1015, NSF SHINE grant 2229138, and NSF Early Career grant 223743. The work of D.H.B. was performed under contract to the Naval Research Laboratory and was funded by the NASA Hinode program. The authors acknowledge the use of data from the Solar Dynamics Observatory (SDO). Courtesy of NASA/SDO and the AIA, EVE, and HMI science teams. Solar Orbiter is a mission of international cooperation between ESA and NASA, operated by ESA. Hinode is a Japanese mission developed and launched by ISAS/JAXA, with NAOJ as domestic partner and NASA and STFC (UK) as international partners. It is operated by these agencies in cooperation with ESA and NSC (Norway). NLFFF extrapolations and data analysis were performed on the Vienna Scientific Cluster (VSC; https://vsc.ac.at/). We thank the Solar group at MSSL for their discussions which helped progress this work.

Appendix
Magnetic Field Extrapolations

We used the flux-conserving spherical polygon intersection reprojection method of The Astropy Collaboration et al. (2022) to generate a grid of photospheric fluxes in Cartesian cylindrical equal area (CEA) coordinates at the bottom boundary of the extrapolation from SDO/HMI data. The size of the domain is large in order to capture the dispersed field associated with the quiescent filament (Figure 10), and the reprojection to a Cartesian CEA system is an approximation of a spherical coordinate domain. Since we were primarily concerned with the central region away from any slightly distorted edges, we find this approximation sufficient. We then performed a potential field extrapolation using the Green's function of T. Sakurai (1982) to provide boundary conditions for the other (side and top) boundaries.

In a volume within these boundaries, we consider a force-free field (e.g., T. Wiegelmann & T. Sakurai 2021), where $\boldsymbol{J} \times \boldsymbol{B} = \boldsymbol{0}$ and $\nabla \cdot \boldsymbol{B} = 0$, $\boldsymbol{J}$ being the electric current and $\boldsymbol{B}$ being the magnetic field. To generate a field which satisfies these equations, we use a physics-informed neural network (PINN) method (M. Raissi et al. 2019), adapted from R. Jarolim et al. (2023). See H. Baty & V. Vigon (2023) for a discussion of the intricacies of extrapolating coronal magnetic fields with PINN methods. When performing a direct extrapolation of $\boldsymbol{B}$ using this method, as in J. McKevitt et al. (2024), we found difficulties maintaining $\nabla \cdot \boldsymbol{B} = 0$. We therefore implemented a vector potential approach, similar to

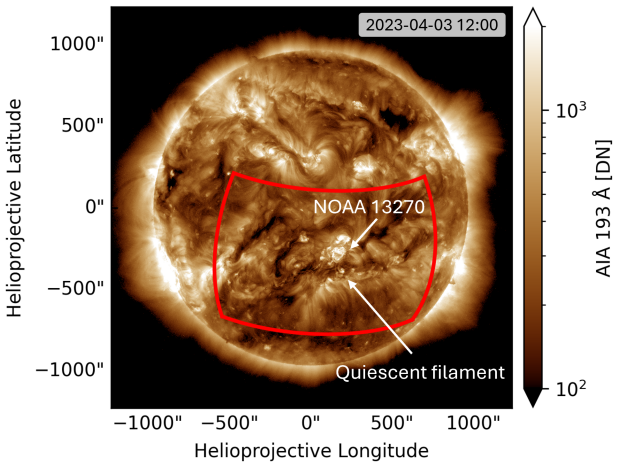

Figure 10. The region of the disk for which NLFFF modeling was performed outlined with a red box. The disk is shown as seen by the SDO/AIA 193 Å channel.

the approach of R. Jarolim et al. (2024) but with some adjustments. In such a method, $\nabla \cdot \boldsymbol{B} = 0$ is inherently satisfied by representing the magnetic field as the curl of a vector potential field, $\boldsymbol{A}$:

$$\boldsymbol{B} = \nabla \times \boldsymbol{A}. \tag{A1}$$

In this paper, we generate this $\boldsymbol{A}$ field with our solver and minimize a loss function from the subsequently calculated $\boldsymbol{B}$ field. Since the divergence of a curl is identically zero, this representation guarantees $\nabla \cdot \boldsymbol{B} = 0$ by construction.

An unconstrained vector potential $\boldsymbol{A}$ can be augmented by an arbitrary scalar field χ such that

$$\boldsymbol{B} = \nabla \times \boldsymbol{A} = \nabla \times (\boldsymbol{A} + \nabla\chi), \tag{A2}$$

given that $\nabla \times \nabla \chi = 0$ (Equation (15) in A. Beresnyak 2023). To handle this "gauge freedom" inherent in the vector potential, we impose the Coulomb gauge condition $\nabla \cdot \boldsymbol{A} = 0$, which we enforced through a Coulomb gauge loss term

$$\mathcal{L}_{\mathrm{CG}} = \frac{1}{N_{\mathrm{CG}}} \sum_{i=1}^{N_{\mathrm{CG}}} (\nabla \cdot \boldsymbol{A}(\boldsymbol{r}_i))^2, \tag{A3}$$

where N_{CG} is the number of collocation points for the gauge condition and $r = (x, y, z)$. These collocation points are randomly sampled locations in the spatial domain where the neural network is penalized for deviating from the constraining equations.

Enforcing the Coulomb gauge also allows us to define the force-free loss (see G. Valori et al. 2016 for details) as

$$\mathcal{L}_{\mathrm{FF}} = \frac{1}{N_{\mathrm{F}}} \sum_{i=1}^{N_{\mathrm{F}}} ||(-\nabla^2 \boldsymbol{A}(\boldsymbol{r}_i)) \times (\nabla \times \boldsymbol{A}(\boldsymbol{r}_i))||^2, \tag{A4}$$

where N_{F} is the number of collocation points for the force-free calculation.

We calculate a boundary loss term $\mathcal{L}_{\mathrm{B}}$, as in R. Jarolim et al. (2023), by taking the mean of all squared differences between the input magnetogram and the bottom boundary of the computed field. We then define our total loss function as

$$\mathcal{L} = \lambda_{\mathrm{B}} \mathcal{L}_{\mathrm{B}} + \lambda_{\mathrm{FF}} \mathcal{L}_{\mathrm{FF}} + \lambda_{\mathrm{CG}} \mathcal{L}_{\mathrm{CG}}, \tag{A5}$$

where λ_{i} are the respective weighting factors.

The training of the neural network involves minimizing the total loss function using the Adam optimizer (D. P. Kingma & J. Ba 2015). When sampling points in our spatial domain for the forward pass, loss computation, backward pass, and network update, we introduce a sampling of collocation points which is gently weighted toward stronger magnetic field locations. This allowed us to better minimize the loss function in the key structures of our large domain.

We evaluate the correctness of our solutions in both their force-freeness and divergence-freeness using the θ_J and f_i terms of M. S. Wheatland et al. (2000). Across our entire simulation volume for all our extrapolations, we found $\theta_J \leqslant 23^\circ$ and $\langle |f_i| \rangle \leqslant 7.5 \times 10^{-6}$, lying in an acceptable range (e.g., M. L. DeRosa et al. 2009).

ORCID iDs

James McKevitt https://orcid.org/0000-0002-4071-5727
Louise Harra https://orcid.org/0000-0001-9457-6200
Gherardo Valori https://orcid.org/0000-0001-7809-0067
Deborah Baker https://orcid.org/0000-0002-0665-2355
Stephanie Yardley https://orcid.org/0000-0003-2802-4381
Sarah Matthews https://orcid.org/0000-0001-9346-8179
Hamish A. S. Reid https://orcid.org/0000-0002-6287-3494
Alexander W. James https://orcid.org/0000-0001-7927-9291
Muriel Stiefel https://orcid.org/0000-0002-8538-3455
David H. Brooks https://orcid.org/0000-0002-2189-9313
Ryan M. Dewey https://orcid.org/0000-0003-4437-0698
Jim M. Raines https://orcid.org/0000-0001-5956-9523
Susan T. Lepri https://orcid.org/0000-0003-1611-227X
Liang Zhao https://orcid.org/0000-0002-5975-7476
Juan Sebastián Castellanos Durán https://orcid.org/0000-0003-4319-2009

References

Antiochos, S. K. 1998, ApJ, 502, L181
Antiochos, S. K., DeVore, C. R., & Klimchuk, J. A. 1999, ApJ, 510, 485
Aulanier, G., Török, T., Démoulin, P., & DeLuca, E. E. 2010, ApJ, 708, 314
Balasubramaniam, K. S., Pevtsov, A. A., Cliver, E. W., Martin, S. F., & Panasenco, O. 2011, ApJ, 743, 202
Baty, H., & Vigon, V. 2023, MNRAS, 527, 2575
Beresnyak, A. 2023, NRL Plasma Formulary (Naval Research Laboratory)
Brooks, D. H., Harra, L., Bale, S. D., et al. 2021, ApJ, 917, 25
Chen, P. F., & Shibata, K. 2000, ApJ, 545, 524
Chen, Y., Przybylski, D., Peter, H., et al. 2021, A&A, 656, L7
Culhane, J. L., Harra, L. K., James, A. M., et al. 2007, SoPh, 243, 19
Dacie, S., Török, T., Démoulin, P., et al. 2018, ApJ, 862, 117
Démoulin, P., Baker, D., Mandrini, C. H., & Van Driel-Gesztelyi, L. 2013, SoPh, 283, 341
DeRosa, M. L., Schrijver, C. J., Barnes, G., et al. 2009, ApJ, 696, 1780
DeVore, C. R., & Antiochos, S. K. 2008, ApJ, 680, 740
Duan, Y., Shen, Y., Zhou, X., et al. 2022, ApJL, 926, L39
Duan, Y., Tian, H., Chen, H., et al. 2024, ApJL, 962, L38
Dulk, G. A. 1985, ARA&A, 23, 169
Edwards, S. J., Parnell, C. E., Harra, L. K., Culhane, J. L., & Brooks, D. H. 2016, SoPh, 291, 117
Engvold, O. 1998, ASPC, 150, 23
Feynman, J., & Martin, S. F. 1995, JGRA, 100, 3355
Golub, L., DeLuca, E., Austin, G., et al. 2007, SoPh, 243, 63
Green, L. M., Török, T., Vršnak, B., Manchester, W., & Veronig, A. 2018, SSRv, 214, 46
Hayes, L. A., Krucker, S., Collier, H., & Ryan, D. 2024, A&A, 691, A190
Hoeksema, J. T., Liu, Y., Hayashi, K., et al. 2014, SoPh, 289, 3483
Jarolim, R., Thalmann, J. K., Veronig, A. M., & Podladchikova, T. 2023, NatAs, 7, 1171
Jarolim, R., Veronig, A. M., Purkhart, S., Zhang, P., & Rempel, M. 2024, ApJL, 976, L12
Kai, K., Melrose, D. B., & Suzuki, S. 1985, Solar Radiophysics: Studies of Emission from the Sun at Metre Wavelengths (Cambridge Univ. Press), 415
Kerdraon, A., & Delouis, J.-M. 1997, in Coronal Physics from Radio and Space Observations, ed. G. Trottet, 483 (Springer), 192
Kingma, D. P., & Ba, J. 2015, arXiv:1412.6980
Kosugi, T., Matsuzaki, K., Sakao, T., et al. 2007, SoPh, 243, 3
Krucker, S., Hurford, G. J., Grimm, O., et al. 2020, A&A, 642, A15
Lemen, J. R., Title, A. M., Akin, D. J., et al. 2012, SoPh, 275, 17
Li, T., Yang, S., Zhang, Q., Hou, Y., & Zhang, J. 2018, ApJ, 859, 122
Li, T., Zhang, J., & Ji, H. 2015, SoPh, 290, 1687
Liu, C., Deng, N., Liu, R., et al. 2015, ApJ, 812, L19
Luoni, M., Mandrini, C., Cristiani, G., & Démoulin, P. 2007, AdSpR, 39, 1382
Lynch, B. J., Antiochos, S. K., DeVore, C. R., Luhmann, J. G., & Zurbuchen, T. H. 2008, ApJ, 683, 1192
Mackay, D. H. 2015, ASSL, 415, 355
Mann, G., Jansen, F., MacDowall, R. J., Kaiser, M. L., & Stone, R. G. 1999, A&A, 348, 614
Markwardt, C. B. 2009, ASPC, 411, 251
Martin, S. F. 1998, SoPh, 182, 107
Masson, S., Pariat, E., Aulanier, G., & Schrijver, C. J. 2009, ApJ, 700, 559
McKevitt, J., Jarolim, R., Matthews, S., et al. 2024, ApJL, 961, L29
McKevitt, J., Matthews, S., Brooks, D., et al. 2025, PASJ, submitted
Metcalf, T. R. 1994, SoPh, 155, 235
Metcalf, T. R., Leka, K. D., Barnes, G., et al. 2006, SoPh, 237, 267

Moore, R. L., & Roumeliotis, G. 1992, in LNP Vol. 309, Eruptive Solar Flares, ed. Z. Švestka, B. V. Jackson, & M. E. Machado (Springer), 69
Moore, R. L., Sterling, A. C., Hudson, H. S., & Lemen, J. R. 2001, ApJ, 552, 833
Murray, M. J., Baker, D., Van Driel-Gesztelyi, L., & Sun, J. 2010, SoPh, 261, 253
Müller, D., St. Cyr, O. C., Zouganelis, I., et al. 2020, A&A, 642, A1
Parenti, S. 2014, LRSP, 11, 1
Pesnell, W. D., Thompson, B. J., & Chamberlin, P. C. 2012, SoPh, 275, 3
Pontin, D. 2011, AdSpR, 47, 1508
Pontin, D. I., Al-Hachami, A. K., & Galsgaard, K. 2011, A&A, 533, A78
Raissi, M., Perdikaris, P., & Karniadakis, G. 2019, JCoPh, 378, 686
Reid, H. A. S., Vilmer, N., Aulanier, G., & Pariat, E. 2012, A&A, 547, A52
Rochus, P., Auchère, F., Berghmans, D., et al. 2020, A&A, 642, A8
Sakurai, T. 1982, SoPh, 76, 301
Schmieder, B., Demoulin, P., Aulanier, G., & Golub, L. 1996, ApJ, 467, 881
Shimizu, T., Imada, S., Kawate, T., et al. 2019, SPIE, 11118, 6
Sterling, A. C., Chifor, C., Mason, H. E., Moore, R. L., & Young, P. R. 2010, A&A, 521, A49
Sterling, A. C., Moore, R. L., Falconer, D. A., & Adams, M. 2015, Natur, 523, 437
Tassev, S., & Savcheva, A. 2017, ApJ, 840, 89
The Astropy Collaboration, Price-Whelan, A. M., Lim, P. L., et al. 2022, ApJ, 935, 167
Tian, H., Harra, L., Baker, D., Brooks, D. H., & Xia, L. 2021, SoPh, 296, 47
Török, T., Aulanier, G., Schmieder, B., Reeves, K. K., & Golub, L. 2009, ApJ, 704, 485
Török, T., Linton, M. G., Leake, J. E., et al. 2024, ApJ, 962, 149
Valori, G., Calchetti, D., Moreno Vacas, A., et al. 2023, A&A, 677, A25
Valori, G., Pariat, E., Anfinogentov, S., et al. 2016, SSRv, 201, 147
Vial, J.-C. 1998, IAUC, 167, 175
Volpara, A., Massa, P., Perracchione, E., et al. 2022, A&A, 668, A145
Wang, H., & Liu, C. 2012, ApJ, 760, 101
Wang, J., & Shi, Z. 1993, SoPh, 143, 119
Wang, Y., & Muglach, K. 2007, ApJ, 666, 1284
Wang, Y.-M., & Sheeley, N. R., Jr. 1999, ApJ, 510, L157
Weberg, M. J., Warren, H. P., Crump, N., & Barnes, W. 2023, JOSS, 8, 4914
Wheatland, M. S., Sturrock, P. A., & Roumeliotis, G. 2000, ApJ, 540, 1150
Wiegelmann, T., & Sakurai, T. 2021, LRSP, 18, 1
Woods, T. N., Eden, T., Eparvier, F. G., et al. 2024, JGRA, 129, e2024JA032925
Wyper, P. F., Antiochos, S. K., & DeVore, C. R. 2017, Natur, 544, 452